Surfaces and Interfaces 44 (2024) 103752

Contents lists available at ScienceDirect

Surfaces and Interfaces

journal homepage: www.sciencedirect.com/journal/surfaces-and-interfaces

Probing molecular arrangements of the organic semiconductor 2,7-Dioctyl [1]benzothieno[3,2- b][1]benzothiophene thin film at the interface by UV Resonant Raman scattering

Tommaso Salzillo [a,*], Jinghai Li [b], Raphael Pfattner [b], Elisabetta Venuti [a], Marta Mas-Torrent [b], Francesco D'Amico [c,*]

[a] Dipartimento di Chimica Industriale "Toso Montanari", and, INSTM-UdR Bologna, Università di Bologna, Viale del Risorgimento 4, Bologna 40136, Italy
[b] Institut de Ciència de Materials de Barcelona, ICMAB-CSIC, Campus UAB, 08193 Bellaterra, Spain
[c] Elettra Sincrotrone Trieste S.C.p.A, S.S. 14km 163,5 in Area Science Park, Basovizza, TS 34149, Italy

ARTICLE INFO

Keywords:
Organic semiconductors
Thin film
Raman spectroscopy
C8-BTBT-C8

ABSTRACT

Raman spectroscopy was employed to investigate nanometric thick films of the organic semiconductor 2,7-Dioctyl[1]benzothieno[3,2-*b*][1]benzothiophene, following a comprehensive vibrational characterization of the compound condensed phases at various excitation wavelengths. UV Raman excitation enabled the characterization of the thin films, revealing that the molecular orientation at the film/air interface is characterized by a different organization and/or a high degree of disorder compared to the bulk phase. The low penetration depth of the UV Raman excitation allows for the retrieval of this information, unlike the XRD data.

1. Introduction

Organic electronics research has grown significantly in the past few years, moving from single crystal-based to more industrially appealing thin film-based devices [1–3]. The interest has been fueled by the many advantages of these systems, which include mechanical flexibility, low cost, and large area manufacturing by solution deposition methods [4].

Many organic compounds have been investigated as candidates for active semiconducting materials, but for many years pentacene and rubrene have acted as market standards, with charge carrier mobilities exceeding that of amorphous silicon [5,6]. However, their chemical stability is low and they oxidize easily in atmospheric conditions, especially when used in solution for film manufacturing. In the last decade, [1]benzothieno[3,2-*b*][1]benzothiophene (BTBT) derivatives have emerged as new references in the field, with excellent electrical performance and high stability in ambient conditions, in solution, and also at relatively high processing temperatures [7–10]. Among the others, 2,7-Dioctyl[1]benzothieno[3,2- *b*][1]benzothiophene (C_8-BTBT-C_8) combines a good solubility with a hole transport exceeding 40 $cm^2\ V^{-1}\ s^{-1}$ in solution processed OFETs [11].

When fabricated using solution methods, C_8-BTBT-C_8 thin films exhibit attractive features such as well-ordered edge-on molecule orientation in a herringbone configuration, which is ideal for 2D charge transport, and large crystalline domains [12]. All of these characteristics have led to the implementation of C_8-BTBT-C_8 in OFETs [13], organic and hybrid bulk heterojunctions [14–16], thermoelectric devices [17] and photo-response transistors [17,18].

Vacuum vapor deposition (PVD) used to be the method of choice to fabricate organic semiconductor (OSC) thin layers because it is a controllable process that allows for the modulation of the many parameters on which the film properties depend, such as deposition rate, substrate temperature, and nominal film thickness [19]. However, in the past two decades, alternative techniques have been adopted, such as spin-coating, blade-coating, dip-coating and bar-assisted meniscus shearing [20], that rely on the formation of the film structure from solution. These methods, that are sought after because of the low fabrication costs, turn out to favor well-defined, two dimensional (2D) networks of a variety of OSC compounds by promoting the molecular self-assembly in liquid surroundings. As a result, the OFETs based on the obtained films may actually outperform their PVD-processed counterparts [21]. Film growth from solution, on the other hand, is dependent on non-equilibrium, difficult-to-control phenomena such as solvent rapid evaporation and crystallization at a solid surface. Because of this, structural characterization of the film is crucial in order to assess its

* Corresponding authors.
E-mail addresses: tommaso.salzillo@unibo.it (T. Salzillo), francesco.damico@elettra.eu (F. D'Amico).

https://doi.org/10.1016/j.surfin.2023.103752
Received 5 October 2023; Received in revised form 22 November 2023; Accepted 11 December 2023
Available online 16 December 2023

crystalline order, homogeneity, and the presence of polymorphic thin film phases. [22,23].

Similar to other methods, the characterization of the films by vibrational spectroscopy often suffers both from the low signal of the thin organic layers and the interference of the substrate.

In the present work we demonstrate how in the Raman technique these difficulties can be overcome by a judicious choice of the excitation source. The investigation has necessarily started from the study of the bulk crystal system as function of the excitation energy, monitoring the Raman scattering response in resonance and off-resonance conditions. Spectra analysis has been assisted by DFT calculations of the vibrational modes. This has allowed us to acquire a good knowledge of the vibrational properties of the C_8-BTBT-C_8 condensed phase, which was still missing. Hence, the application of UV Raman on nanometer thick films reproducing the layer architecture of the C_8-BTBT-C_8 OFETs has enabled the detection of their spectra with a high signal-to-noise ratio. As an added bonus, the employed excitation wavelength is strongly absorbed by the material and thus has small penetration depth. This in turn allows to selectively observe features characteristic of the most external layers of the film. In fact, in contrast to the X-ray diffraction technique, which only probes the ordered C_8-BTBT-C_8, the low penetration depth of the UV Raman excitation enabled the probing of the molecular orientation at the film/air interface, revealing a different organization of the molecules on the OSC disordered surface layer.

2. Material and methods

2.1. Sample preparation

Single crystals were prepared by dissolving C_8-BTBT-C_8 (Sigma Aldrich, purity >99%) in chlorobenzene (CB, Sigma-Aldrich HPLC grade) to a 2% w/w concentration. The solution was then heated and kept at 100 °C for one hour to ensure that the organic compound was fully dissolved, and then left to evaporate slowly at room temperature. After a few weeks, plate-like colorless crystals of millimetric size were obtained. Thin films were fabricated by the bar-assisted meniscus shearing (BAMS) technique [24–26], depositing a 2% w/w chlorobenzene solution of C_8-BTBT-C_8 on Si/SiO_2 substrates purchased from Si-Mat (SiO_2 thickness of 200 nm), previously cleaned with acetone and isopropanol and then dried under a nitrogen flow. The temperature of the hot bed of the BAMS apparatus was kept constant at 105 °C, and the shearing speed was fixed at the 10 mm s^{-1}, value optimized in previous works [27,28].

2.2. Thin film characterization

Polarized optical microscopy (POM) images were taken with Olympus BX51 microscope equipped with polarizer and analyzer at 90° in reflection mode, as done elsewhere [29]. Film crystallinity and polymorphic structure were characterized by X-ray diffraction (XRD) examining the out-of-plane diffraction peaks in Φ/2Φ configuration (Siemens d-5000 diffractometer) employing Cu Kα1 radiation (λ = 1.5406 Å) at room temperature. The peaks were fitted to a Voigt function. Film topography, thickness and roughness were extracted from atomic force microscopy (AFM) images (Keysight 5100 system from Agilent) taken in constant amplitude dynamic mode. The images were analyzed with the Gwyddion 2.52 software. The thickness of the films was measured by AFM using the step-edge method. A portion of the OSC film was removed by scratching it with a needle down to the substrate. The analysis of the cross-section profile through the scratch was then used to determine the thickness of the film.

2.3. Raman

Raman measurements were carried out at the IUVS beamline at Elettra Synchrotron radiation facility, in Trieste. A detailed description of the experimental apparatus is reported elsewhere [30]. For the measurements at 532 nm and 633 nm we employed, in backscattering configuration, a $f = 750$ mm single stage Czerny-Turner spectrometer (Andor, SR-750-A) equipped with an 1800 lines/mm holographic reflection grating and a back-illuminated palter cooled CCD (Andor, DU420A-BU2). The final spectra at 532 nm were obtained by merging 20 spectra collected over different wavenumber ranges while 6 spectra were needed for the merging at 633 nm. Count rate was set at 10 s for each spectrum at 532 nm and 5 min for each spectrum at 633 nm. Final spectra bandwidth was kept at 3 cm^{-1}.

A backscattering configuration, geometrically identical to the one used at 532 nm and 633 nm, was used to collected the Raman signal at 266 nm, in a Czerny-Turner single stage $f = 750$ mm spectrometer (Trivista, Princeton Instruments) coupled with a Peltier cooled back-thinned CCD (Princeton Instruments). Count rate was 15 min for each spectrum. Final spectra bandwidth was 8 cm^{-1}. The background has been removed from all spectra.

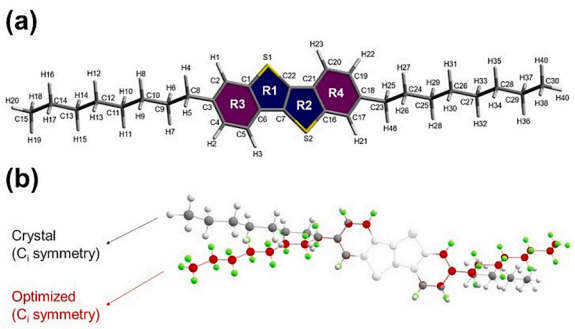

Fig. 1. (a) Chemical structure of C_8-BTBT-C_8 as derived from quantum mechanics simulations. The figure reports the labelling adopted in the text for atoms and aromatic rings. (b) Chemical structure of C_8-BTBT-C_8 before and after the geometrical optimization obtained by quantum mechanics calculations.

2.4. Simulations

Simulated Raman spectra were obtained from the Raman activities and normal mode frequencies calculated by means of a hybrid DFT method. Specifically, the three-parameter (B3LYP) hybrid functional with Becke '88 exchange [31,32] and Lee-Yang-Parr correlation [33] was chosen, together with the Karlsruhe double-zeta valence (def2-SVP) basis set [34,35], employing a scaling factor of 0.9671 [36]. To maintain the molecular structure as close as possible to that of films, the starting geometry for a single C_8-BTBT-C_8 molecule was taken from the XRD data [37,38], and it was then optimized with the constraint of the C_i site symmetry of C_8-BTBT-C_8 in the crystal (Fig. 1). This ensures that the calculated active Raman modes of symmetry A_g are also the active ones in the crystal. Noteworthy, each mode in the crystal gives rise to an A_g/B_g doublet as a result of the Davydov splitting effect, which however is unlikely to be detected at the spectral resolution of the experiments.

The comparison between the original geometry in the crystal and the optimized one is shown in Fig. 1, panel (b). The optimization procedure slightly folds the lateral chains, while negligible variations occur in the aromatic ring conformation.

The final simulated spectra are rendered as the sum of Voigt curves having both Lorentzian and Gaussian FWHMs of 3 cm^{-1} and area proportional to:

$$A_i = \frac{(\upsilon_0 - \upsilon_i)^4 R_i}{\upsilon_i \left[1 - \exp\left(-\frac{hc\upsilon_i}{k_B T}\right)\right]}$$

where R_i is the calculated Raman scattering activity, υ_0 the frequency of the excitation source (in wavenumber units), $T = 300$ K the temperature

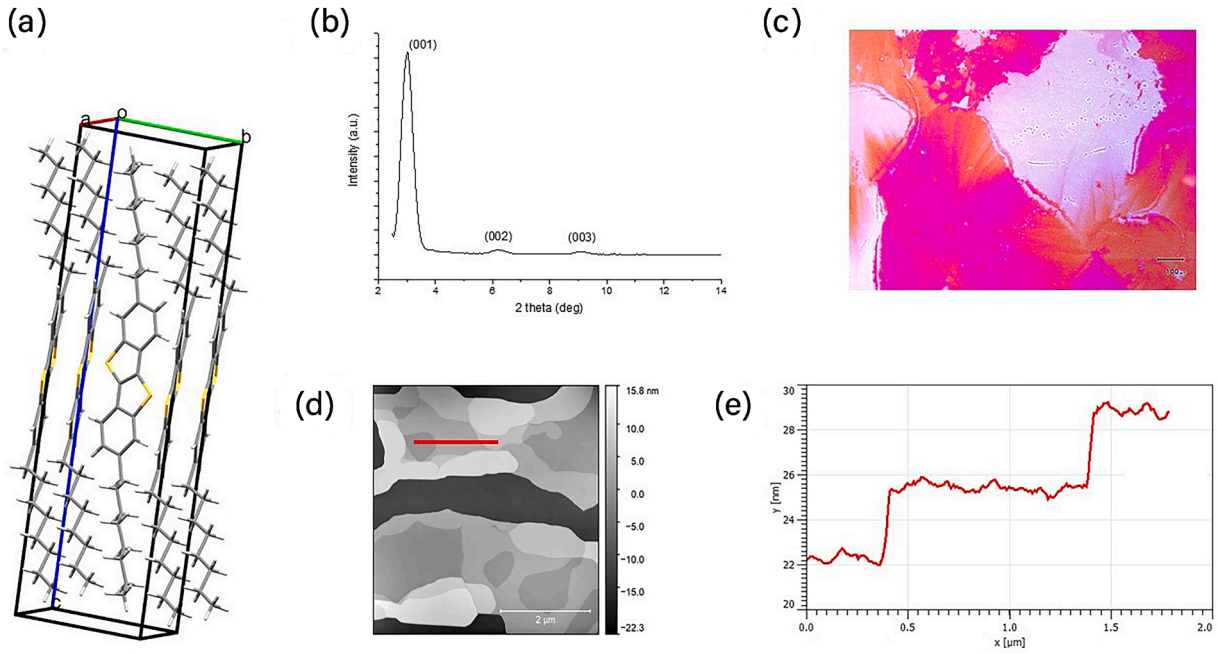

Fig. 2. (a) Crystal packing configuration; (b) XRD of C_8-BTBT-C_8 thin films showing the (00x) family reflection peaks indicating the *ab* crystal plane parallel to the surface; (c) POM picture of the thin film obtained by BAMS; (d) AFM topography of C_8-BTBT-C_8 thin films fabricated by the BAMS on Si/SiO_2; (e) Line profile extracted from the AFM topography (red line).

and υ the calculated normal mode wavenumber [39,40]. Calculations were performed with the Orca 5.0 software package [41].

3. Results and discussion

3.1. Crystal structure characterization

C_8-BTBT-C_8 crystal structure was solved by Izawa and coworkers [42] by single-crystal X-ray analysis. The compound crystallizes in the monoclinic system, with space group $P2_1/a$ and $Z = 2$ molecules per cell (see Supplementary file for the lattice parameters). The molecular arrangement (Fig. 2, panel (a)) is characterized by a lamella-like alternating structure of alkyl chains and BTBT aromatic core layers along the *c* crystallographic axis. The BTBT aromatic cores are arranged in a herringbone configuration, thus yielding an ideal packing for two-dimensional charge transport in the *ab* plane. Out-of-plane XRD measurements of a drop cast single crystal show the peaks belonging to the (00n) family reflections, indicating that the platelet flat face corresponds to the *ab* plane with the *c* axis perpendicular to the substrate surface, as shown in Fig. 2 panel (b) [42].

Thin films were prepared by the solution shearing method BAMS as described in the experimental section. As reported previously [27–29], C_8-BTBT-C_8 films deposited by this technique consist of homogeneous layers of the OSC as shown by optical microscopy in crossed polarized configuration (Fig. 2 Panel (c)), with crystalline domains randomly oriented in plane and the crystallographic *c*-axis parallel to the substrate normal, as demonstrated by out-of-plane XRD measurements and thickness values estimated by AFM analysis below 15 nm (Fig. 2 panel (e)) [27–29,43].

The randomly organized polycrystalline domains show different heights with steps of ~3 nm as reported for the red trace on the AFM image and the step profile of panels d and e of Fig. 2, respectively. Such value nearly corresponds to the molecular length of a C_8-BTBT-C_8 molecule, confirming the standing-up organization of the molecules in the crystalline domains. Thus, the molecular arrangement in the thin film does coincide with the one of the single crystals, which have a platelet-like morphology. Because of this, the same *ab* crystal face gets probed in the Raman experiments of all samples: bulk, thin films and even polycrystalline powders, as these are made of micrometric platelets lying on such face.

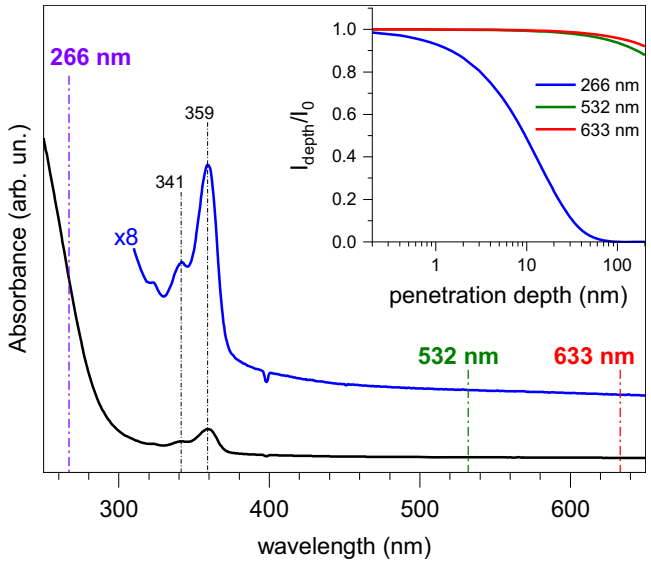

Fig. 3. Experimental UV–Vis absorption spectrum of C_8-BTBT-C_8 thin film on quartz substrate. The dip at 400 nm is an artifact resulting from the change of lamp in the spectrometer. The inset reports the laser penetration depth inside C8-BTBT-C8, calculated based on the absorption spectrum.

3.2. Raman characterization

To ascertain the possible occurrence of resonant Raman effects, the absorption spectrum of C_8-BTBT-C_8 is presented in Fig. 3, where the excitation wavelengths used in the Raman studies (namely 633 nm, 532 nm, and 266 nm) are reported as dotted vertical lines.

The C_8-BTBT-C_8 absorption spectrum is characterized by two peaks

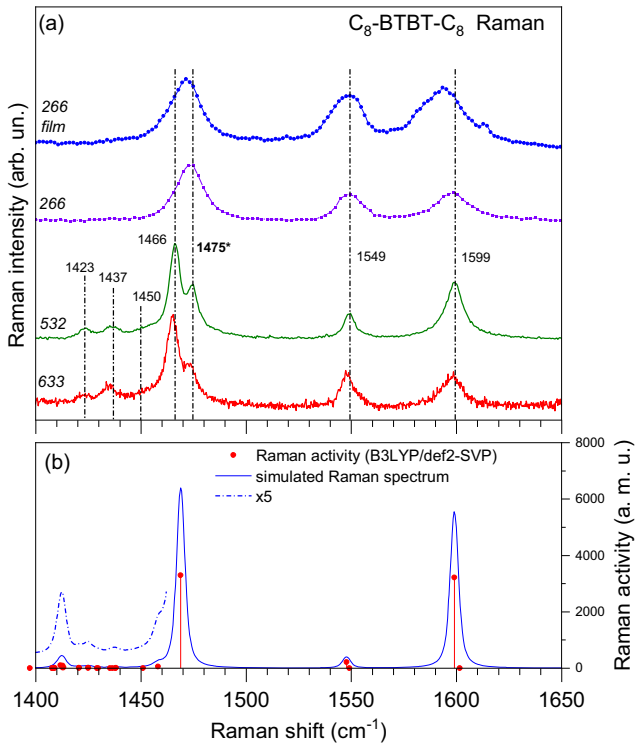

Fig. 4. Panel (a), Raman spectra of C_8-BTBT-C_8 collected employing an excitation wavelength of 633 nm (red curve), 532 nm (green curve) and 266 nm (violet curve), in the wavenumber range of 1400–1650 cm^{-1}. The Raman spectrum of the C_8-BTBT-C_8 thin film, collected at 266 nm is also reported (blue curve). Spectra have been normalized in intensities to the peak at 1475 cm^{-1}. Panel (b), simulated Raman spectrum of C_8-BTBT-C_8, in the wavenumber range of 1400–1650 cm^{-1}. The Raman activity, as derived from simulations, is also reported.

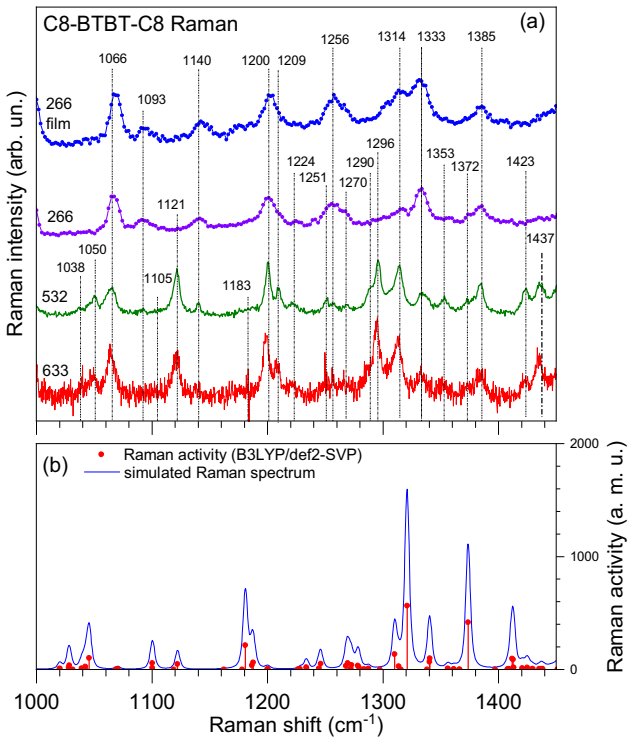

Fig. 5. Panel (a), Raman spectra of C_8-BTBT-C_8 collected employing an excitation wavelength of 633 nm (red curve), 532 nm (green curve) and 266 nm (violet curve), in the wavenumber range of 1400–1650 cm^{-1}. The Raman spectrum of the C_8-BTBT-C_8 thin film, collected at 266 nm is also reported (blue curve). Panel (b), simulated Raman spectrum of C_8-BTBT-C_8, in the wavenumber range of 1100–1450 cm^{-1}. The Raman activity, as derived from simulations, is also reported.

at 359 nm and 341 nm, while below 300 nm a strong increase of absorbance occurs. According to the literature [29], these peaks result from electronic transitions occurring within the BTBT core, *i.e.* the compound's chromophore group. Overall, the spectrum changes very little in comparison to the parent molecule, with the first transition being the symmetry allowed HOMO-LUMO [44], followed by more, still involving the electronic density of the aromatic rings. The excitations at 633 nm and 532 nm lie far from the absorptions, hence the corresponding Raman scatterings can be treated as normal Raman. On the contrary, when the excitation is moved to λ_{exc} = 266 nm, *i.e.* the Resonant Raman (RR) conditions for the transitions involving the BTBT core should be satisfied. In general, a vibration will be RR active when the electronic excitation produces a change in either bond length or angle of the atoms involved in the excited state compared to ground state. Thus, the effect is expected to show especially for those modes localized on the BTBT hetero-aromatic core of the molecule, *i.e.* containing the π electron system, which are expected to gain strength in comparison to those originating from the lateral aliphatic chains.

An estimate of the penetration depth of excitation source is obtained by following Hong and co-authors [45]: given $I_0(\lambda_{exc})$ the intensity of the source and $I_{depth}(l, \lambda_{exc})$ the intensity at depth l from the film interface, their ratio can be computed as:

$$\frac{I_{depth}(l,\lambda_{exc})}{I_0(\lambda_{exc})} = e^{-2.303\times\alpha(\lambda_{exc})\times l}$$

where $\alpha(\lambda_{exc})$ is the absorption coefficient at λ_{exc}. As the C_8-BTBT-C_8 absorption coefficient is known from the literature to be $\approx 5 \times 10^4$ cm^{-1} at λ_{exc} = 359 nm [46], it can be deduced at other wavelengths from the absorption spectrum of Fig. 3 (specifically 3.1 × 10^5 cm^{-1} at 266 nm, 2.8 × 10^3 cm^{-1} at 532 nm and 1.8 × 10^3 cm^{-1} at 633 nm). This allows for a safe estimate of the intensity ratios as a function of the penetration depth l for the three λ_{exc} employed in this work, as reported in the curves of the inset of Fig. 3. The 266 nm curve clearly shows that the intensity of this excitation decays within a few nanometres from the film surface, differently to what occurs for the excitations at 532 nm and 633 nm. This makes the 266 nm excitation more sensitive to the surface structural features and molecular arrangements than those in the visible range, which are instead more suited to infer information about bulk conditions.

In the following, the vibrational analysis of C_8-BTBT-C_8 bulk and film phases based on the Raman spectra collected at different excitation energy is reported. A detailed analysis must include the 2800–3100 cm^{-1} wavenumber range, where the C—H stretching modes are found. The modes observed in such interval are not relevant to the scope of this work, but for the sake of completeness these results are given in the supplementary files along with the corresponding DFT simulations (see Figure S1 and Table S1).

In Fig. 4 the Raman spectra collected at the excitation wavelengths λ_{exc} = 633, 532 and 266 nm on C_8-BTBT-C_8 crystalline powder are compared to the thin film spectrum recorded with the only λ_{exc} = 266 nm over the range 1400–1650 cm^{-1}. Because of a poor scattering volume, it was not possible to obtain Raman spectra from the film neither employing λ_{exc} = 532 nm nor 633 nm. Instead, at λ_{exc} = 266 nm, the combination of resonant effects and lower wavenumber act to compensate the low volume and a spectrum with a high signal to noise ratio can be collected. The 633 nm and 532 nm excitation spectra of the powder are characterized by the presence of peaks at 1599, 1549, 1466, 1437 and 1423 cm^{-1}. Moving to λ_{exc} = 266 nm, the bands get broader because of the lower spectral resolution, but it is clear that only three peaks at 1599 cm^{-1}, 1549 cm^{-1} and 1475 cm^{-1} are left.

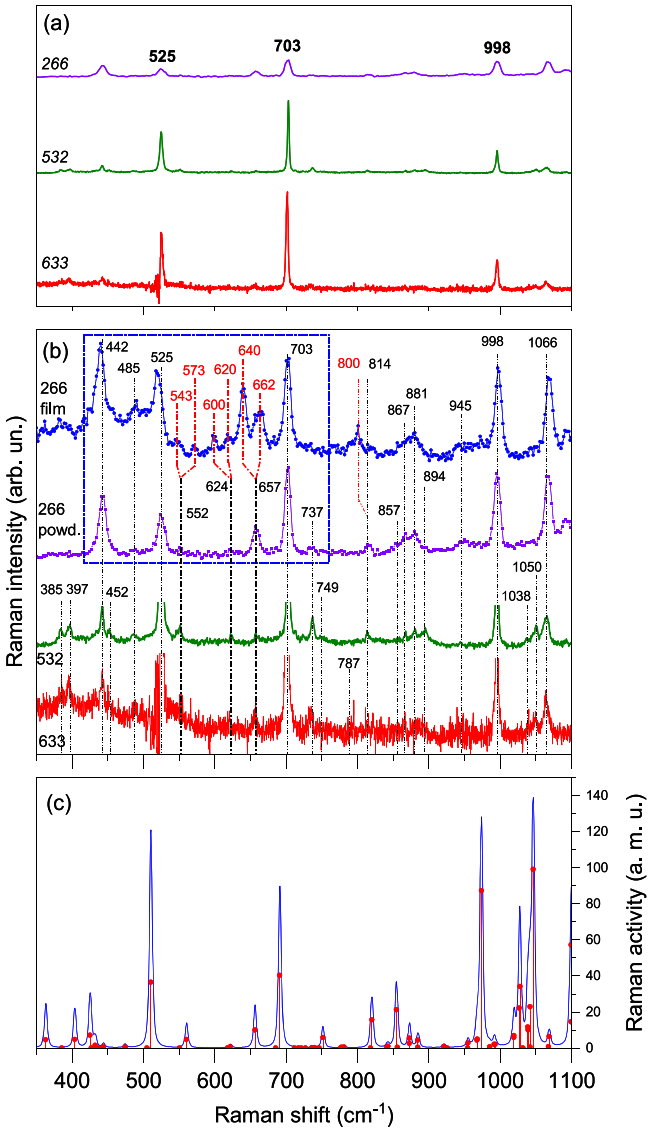

Fig. 6. Panel (a), Raman spectra of C_8-BTBT-C_8 powder collected with λ_{exc} = 633nm (red curve), 532 nm (green curve) and 266 nm (violet curve), in the wavenumber range of 350–1100 cm^{-1}. Panel (b), same of panel (a) but with the spectra at λ_{exc} = 633and 532 nm vertically cut in order to enhance the behavior of the less intense peaks The Raman spectrum of the C_8-BTBT-C_8 thin film, collected at λ_{exc} = 266 nm is also reported (blue curve). Panel (c), simulated Raman spectrum of C_8-BTBT-C_8, in the wavenumber range of 1100–1450 cm^{-1}. The Raman activity, as derived from simulations, is also given.

Notwithstanding some small frequency shifts, the thin film spectrum corresponds to that of the crystal, with the maximum at 1549 cm^{-1} that does not change, whereas those lying at 1599 and 1475 cm^{-1} in the powder downshift to 1595 and 1472 cm^{-1}, respectively, in the film. To aid with reliable vibrational assignments, the simulated Raman spectra of C_8-BTBT-C_8 are reported on the panel (b) of Fig. 4. The analysis shows that the scattering at 1599 cm^{-1} corresponds to a symmetric stretching involving C atoms of the lateral R4 and R3 benzo rings (see Fig. 1 and Table S1 in supplementary files for the atom numbering). The scattering at 1549 cm^{-1} can instead be assigned to a combination of C—C stretching involving mostly the internal R1 and R2 thiophene rings, with some contributions also of the C atoms in R3 and R4. Similar assignments can be made for the 1466 cm^{-1} and 1475 cm^{-1} vibrations, both corresponding to C—C stretching modes of the thiophene rings. The agreement with the scaled [36] simulated values for these vibrations (1598, 1547, 1468 and 1458 cm^{-1}, respectively) is pretty good. Note that the band at 1475 cm^{-1} grows in intensity with respect to that at 1599 cm^{-1} and 1548 cm^{-1} from λ_{exc} = 532 nm to λ_{exc} = 266 nm, possibly as a result of RR effect acting differently on these modes [47,48]. The simulations allow for the assignment of two more peaks at 1437 cm^{-1} and 1423 cm^{-1} of Fig. 5 to C—H_2 scissoring vibrations, mainly localized on the lateral aliphatic chains. This explains the absence of such signals in the λ_{exc} = 266 nm spectrum, where, because of the resonance conditions, the vibrational features originating from the aromatic rings get enhanced and dominate over the others.

The C_8-BTBT-C_8 Raman spectra between 1000 cm^{-1} and 1450 cm^{-1} are reported, In Fig. 5, with a scheme similar to that of Fig. 4. The scattering at 1385 cm^{-1} (simulated at 1372 cm^{-1}) is assigned to a combination of in-plane C—H bending in R3 and R4 and of C—C stretching also occurring within R3 and R4. The nature of this vibration explains why, as a result of resonance effects, its intensity increases at λ_{exc} = 266 nm with respect to the bands of the scissoring modes lying at 1423 and 1437 cm^{-1}. The peak at 1353 cm^{-1}, visible at λ_{exc} = 532 nm and very weak at λ_{exc} = 266 nm, can be assigned to a combination of modes that includes C—H wagging in the lateral chains. The peak at 1333 cm^{-1} (simulated at 1320 cm^{-1}), observed at all excitations and also displaying an increase of its relative intensity from visible to UV excitation, can be associated to a combination of C—C stretching in R3 and R4 together with wagging and twisting motions involving several CH_2 groups of the lateral chains. Moving to lower wavenumbers, three well defined peaks can be found at 1314, 1296 and 1290 cm^{-1} both at λ_{exc} = 532 nm and 633 nm. The first can be associated to R1 and R2 C—C and S-C stretching vibrations, the second to twisting CH_2 vibrations in lateral chains and finally the third one to combinations of both CH_2 wagging and twisting in the same lateral chains. Note also that the intensity ratio between the1314 cm^{-1} and 1333 cm^{-1} is larger in the film compared to the crystal, resulting in a broader convolution.

The scattering at 1256 cm^{-1}, strong also at λ_{exc} = 266, can be assigned to lateral chains CH_2 wagging and twisting motions respectively, while those at 1251 cm^{-1} and 1223 cm^{-1} originate from a combination of in plane C—H bending vibrations in R3 and R4 and lateral chains CH_2 wagging and twisting. Similar assignments can be made for the peaks at 1209, 1200 and 1183 cm^{-1}. The vibration at 1140 cm^{-1} is mainly a bending taking place inside R3 and R4. Accordingly, its intensity is high also at λ_{exc} = 266266 nm, unlike the peaks at 1121 cm^{-1} and 1105 cm^{-1} which are not detected at this excitation and correspond to wagging and twisting vibrations in the lateral chains. A similar assignment can be made for the peak at 1093 cm^{-1}. The intense peak at 1066 cm^{-1} is assigned to R1 and R2 C—C stretching combined with R3 and R4 O—H bending, while the less intense 1050 and 1038 cm^{-1} peaks pertain to C—C stretching in the lateral chains. In the 1038 cm^{-1} peak, chain C—C stretching are combined with CH_2 wagging. As no displacements in the aromatic ring atoms occur, these two vibrations do not get enhanced in the λ_{exc} = 266 nm spectrum.

In Fig. 6 the Raman spectra of C_8-BTBT-C_8 in the wavenumber range of 350–1100 cm^{-1} are shown. A detailed assignment of this very crowded energy interval, which also includes the fingerprint region of the compound, can be found in the SI. For the sake of clarity here we will focus on the relevant differences between the spectra recorded at the various excitation wavelengths. In this range the spectral behavior at λ_{exc} = 633and 532 nm is remarkably different from that at λ_{exc} = 266 nm. Specifically, (see panel (c)) the three Raman peaks at 996, 703 and 525 cm^{-1} dominate the spectra at 532 and 633 nm but their relative drop significantly at λ_{exc} = 266 nm.

Since the spectra have been normalized to the intensity of the peaks at 1475 cm^{-1}, this behavior could be ascribed to a large increase of the Raman cross sections of the normal modes corresponding to the latter scatterings at λ_{exc} = 266 nm.

The spectral region between 400 cm^{-1} and 700 cm^{-1} is also where crystalline powder and thin film spectra at λ_{exc} = 266 nm most differ, as the film generally displays in the broader and more numerous bands, accompanied by frequency shifts. Indeed, the features found in the

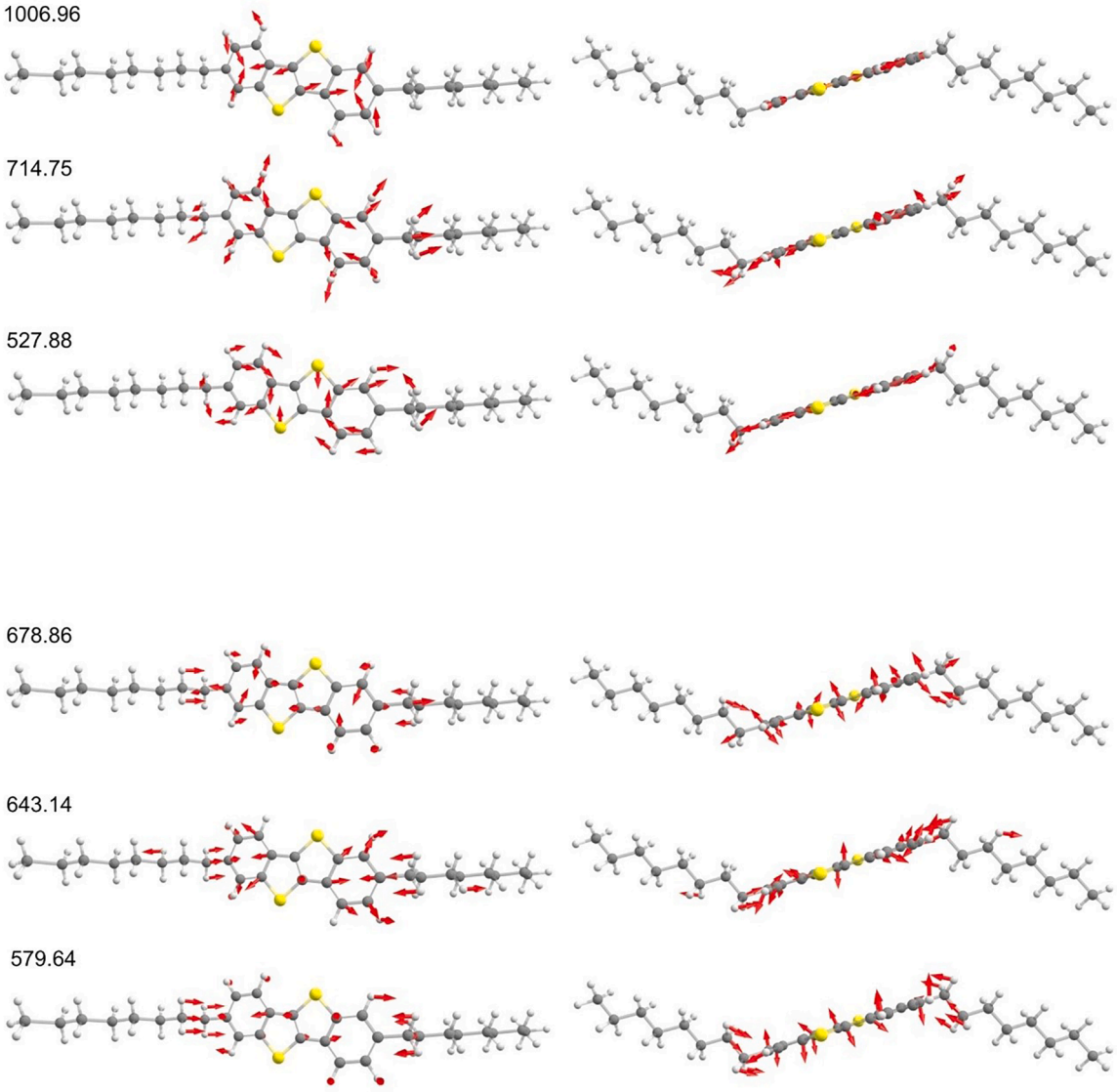

Fig. 7. Schematic representation of atoms displacements in some specific normal modes. The simulated wavenumber is reported.

crystal at 657 cm^{-1}, 624 cm^{-1} and 552 cm^{-1} change in the thin film. Specifically, instead of these bands it is now possible to detect bands at 662 cm^{-1} and 640 cm^{-1}, 620 cm^{-1} and 600 cm^{-1} and finally at 547 and 573 cm^{-1}. The comparison with the simulated spectrum allows to assign the three crystal peaks to the simulated normal modes at 678.86 cm^{-1}, 643.14 cm^{-1} and 579.64 cm^{-1}. Interestingly, as highlighted in Fig. 7, such normal modes correspond to out-of-plane bendings within the aromatic rings, a characteristic that will be discussed below. Conversely, at $\lambda_{exc} = 266$ nm the three bands at 998 cm^{-1}, 703 cm^{-1} and 525 cm^{-1} are the same both in crystal and in the thin film. They can be assigned to the simulated normal modes respectively at 1006.96 cm^{-1}, 714.75 cm^{-1} and 527.88 cm^{-1}, ring bendings and deformations which have no out-of-plane displacement components. (Fig. 7).

Thus, altogether, the spectra of bulk and films display remarkable differences in the compound fingerprint region, with the films showing more bands and a general increase of their overall intensity. In this energy range the molecular vibrations might be strongly coupled to collective lattice phonons, as the mixed character of many molecular modes has been computationally demonstrated for another BTBT derivative, namely C_8O-BTBT-OC_8. The molecular disorder arising from the lower degree of crystallization of the films compared to the crystal results in an energy distribution of the mixed modes which are detected as band broadenings and shifts. This applies especially to the flexible alkyl chains, whose conformational and packing arrangement distributions in the film are likely to bring about also the energy distribution of the associated vibrational modes, with symmetry lowering.

A more important source of information concerning the structural and morphological characteristics of the film disorder is provided by the presence of the bands of the out-of-plane vibrations in the films in comparison with the crystalline samples, at all excitation wavelengths and in both the powder and the single crystals. The increased intensity can be explained by assuming a molecular symmetry lowering which makes Raman active some vibrational modes that are intrinsically weak in the C_{2h} symmetry of the crystal. As an alternative, the activation of some specific out-of plane vibrations can be ascribed to a different molecular orientation with respect to the exciting electric field. Crystal platelets and film share, as pointed out before, the same lattice and the same lattice orientation with respect to the incoming beam, directed perpendicular to the *ab* crystal face. The UV $\lambda_{exc} = 266$ nm excitation has two characteristics: it has a shorter penetration depth in the material than higher wavelengths; it gets strongly absorbed in the first layers of the film. The resulting Raman spectra selectively provide information on the layers at the air interface, as the bulk of the material cannot significantly contribute to the overall scattering. Therefore, the

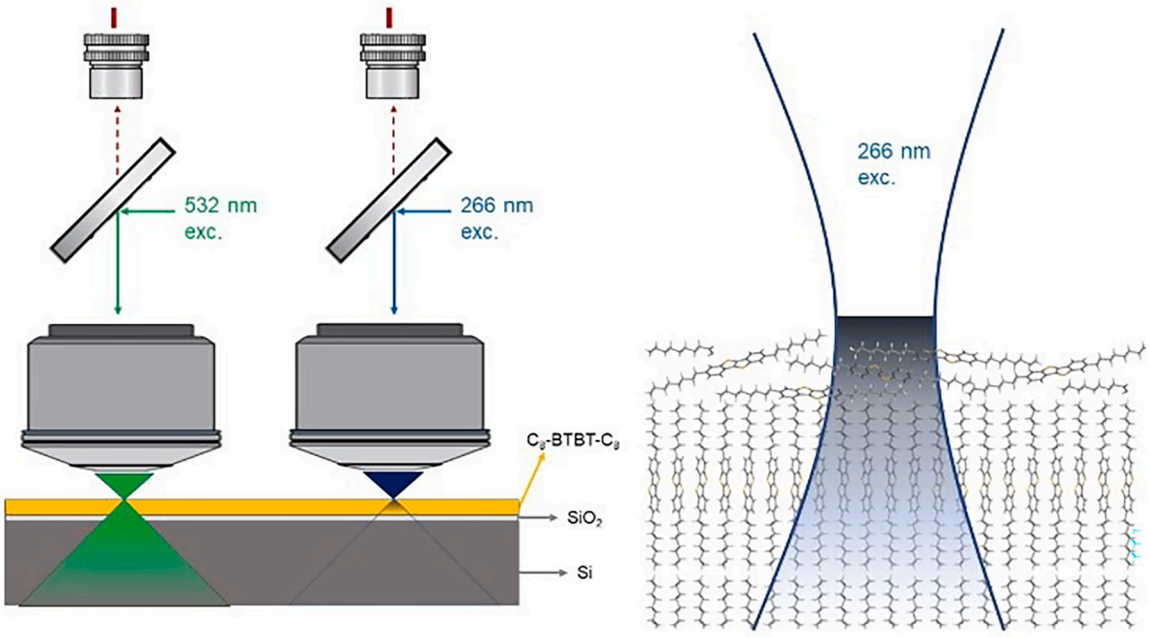

Fig. 8. Panel (a), schematic representation of the different volume scattering investigated by means of 266 nm and 532 nm on a C_8-BTBT-C_8. Panel (b), schematic representation of the C_8-BTBT-C_8 interface investigated by means of 266 nm excitation wavelength.

enhancement of the out-of plane vibrations is due to molecules present in the most external layers of films, oriented differently from those forming the ordered crystal packing of the deeper layers. Such enhancement is compatible with molecules whose cores are not aligned anymore with the *c* crystallographic axis, but stand either tilted or lie flat at the air interface, which implies modifications, even if slight, of the intermolecular interaction patterns and of the molecular geometries, resulting in band broadening, frequency shifts and possibly breaking of symmetry selection rules. It should be noted that the range below 550 cm^{-1} includes modes of the flexible molecular lateral chains, whose conformation is easily influenced by changes of inter-molecular interaction patterns.

The adopted experimental setup is illustrated in Fig. 8, where the schematic representation of the measurement conditions at two different excitation wavelengths helps explaining the origin of the spectral differences observed in the bulk and film spectra at $\lambda_{exc} = 266$ nm and were a sketch of the disordered molecular arrangements at the film-air interface is given.

4. Conclusions

Raman spectroscopic characterization has great potential for the chemical and structural identification of organic semiconductors in thin films. However, such investigation is often prevented in films only few nanometres thick, such as those used in real devices, due to the limited scattering volumes, which make cumbersome the acquisition of good quality spectra.

In this study, we report on the Raman characterization of the benchmark C_8-BTBT-C_8, semiconductor. Non-resonant and resonant Raman conditions were tested in the detailed vibrational characterization of the semiconductor condensed phase. Most importantly, the employment of the 266 nm excitation wavelength finally allowed for the measurements of the spectra in the thin film phases, in fact impossible to obtain with the other excitation's wavelengths tested in this work. Notwithstanding the expected increase of the scattering intensity due to the use of the UV excitation, the intensity enhancement, recorded both in film and crystals, also derives from a Raman resonant effect which selectively involves modes of the chromophore group of the molecule. The results are strongly in support to seek such conditions to have access to the study of the vibrational features of films, as a source of information of their characteristics of order and presence of defects.

CRediT authorship contribution statement

Tommaso Salzillo: Conceptualization, Methodology, Investigation, Writing – original draft, Formal analysis. **Jinghai Li:** Investigation. **Raphael Pfattner:** Writing – review & editing. **Elisabetta Venuti:** Resources, Writing – review & editing, Supervision, Formal analysis. **Marta Mas-Torrent:** Resources, Writing – review & editing, Supervision. **Francesco D'Amico:** Conceptualization, Methodology, Resources, Investigation, Supervision, Writing – original draft, Formal analysis.

Declaration of Competing Interest

The authors declare that they have no known competing financial interests or personal relationships that could have appeared to influence the work reported in this paper.

Data availability

Data will be made available on request.

Acknowledgments

T.S. thanks the Programma per Giovani Ricercatori "Rita Levi Montalcini" year 2020 (grant PGR20QN52R) of the Italian Ministry of University and Research (MUR) for the financial support. T. S. and F. D. acknowledge CERIC-ERIC for providing access to the Elettra IUVS-OFF beamline (beamtime number 20187028). J. L., R. P. and M. M-T. also a acknowledge. funding from MCIN/AEI/10.13039/501100011033/ERDF,UE with projects GENESIS PID2019–111682RB-I00 and SENSATION PID2022–141393OB-I00, and through the "Severo Ochoa" Programme for Centers of Excellence in R&D (FUNFUTURECEX2019–000917-S) and the Generalitat de Catalunya (2021-SGR-00443). R.P. acknowledges support from the Ramón y Cajal Fellowship (Ref. RyC2019–028474-I). This work has been supported by the project "POLYPHON - Polymorph screening to enable electron-

phonon coupling engineering in organic semiconductors" funded by the MUR Progetti di Ricerca di Rilevante Interesse Nazionale (PRIN) Bando 2022 - grant 2022XZ2ZM8.

Supplementary materials

Supplementary material associated with this article can be found, in the online version, at doi:10.1016/j.surfin.2023.103752.

References

[1] X. Ren, F. Yang, X. Gao, S. Cheng, X. Zhang, H. Dong, W. Hu, Organic field-effect transistor for energy-related applications: low-power-consumption devices, near-infrared phototransistors, and organic thermoelectric devices, Adv. Energy Mater. 8 (2018), 1801003, https://doi.org/10.1002/aenm.201801003.

[2] W. Tang, Y. Huang, L. Han, R. Liu, Y. Su, X. Guo, F. Yan, Recent progress in printable organic field effect transistors, J. Mater. Chem. C 7 (2019) 790–808, https://doi.org/10.1039/C8TC05485A.

[3] Z.A. Lamport, H.F. Haneef, S. Anand, M. Waldrip, O.D. Jurchescu, Tutorial: organic field-effect transistors: materials, structure and operation, J. Appl. Phys. 124 (2018), 071101, https://doi.org/10.1063/1.5042255.

[4] H. Sirringhaus, Device physics of solution-processed organic field-effect transistors, Adv. Mater. 17 (2005) 2411–2425, https://doi.org/10.1002/adma.200501152.

[5] R.W.I. de Boer, M.E. Gershenson, A.F. Morpurgo, V. Podzorov, Organic single-crystal field-effect transistors, Phys. Status Solidi A 201 (2004) 1302–1331, https://doi.org/10.1002/pssa.200404336.

[6] D.J. Gundlach, Y.Y. Lin, T.N. Jackson, S.F. Nelson, D.G. Schlom, Pentacene organic thin-film transistors-molecular ordering and mobility, IEEE Electron Device Lett. 18 (1997) 87–89, https://doi.org/10.1109/55.556089.

[7] W. Wei, C. Yang, J. Mai, Y. Gong, L. Yan, K. Zhao, H. Ning, S. Wu, J. Gao, X. Gao, G. Zhou, X. Lu, J.-M. Liu, High mobility solution-processed C8-BTBT organic thin-film transistors via UV-ozone interface modification, J. Mater. Chem. C 5 (2017) 10652–10659, https://doi.org/10.1039/C7TC03794E.

[8] T. Shen, H. Zhou, X. Liu, Y. Fan, D.D. Mishra, Q. Fan, Z. Yang, X. Wang, M. Zhang, J. Li, Wettability control of interfaces for high-performance organic thin-film transistors by soluble insulating polymer films, ACS Omega 5 (2020) 10891–10899, https://doi.org/10.1021/acsomega.0c00548.

[9] T. Endo, T. Nagase, T. Kobayashi, K. Takimiya, M. Ikeda, H. Naito, Solution-processed dioctylbenzothienobenzothiophene-based top-gate organic transistors with high mobility, low threshold voltage, and high electrical stability, Appl. Phys. Express 3 (2010), 121601, https://doi.org/10.1143/APEX.3.121601.

[10] Y. Huang, J. Sun, J. Zhang, S. Wang, H. Huang, J. Zhang, D. Yan, Y. Gao, J. Yang, Controllable thin-film morphology and structure for 2,7-dioctyl[1]benzothieno[3,2-*b*][1]benzothiophene (C8BTBT) based organic field-effect transistors, Org. Electron. 36 (2016) 73–81, https://doi.org/10.1016/j.orgel.2016.05.019.

[11] Y. Yuan, G. Giri, A.L. Ayzner, A.P. Zoombelt, S.C.B. Mannsfeld, J. Chen, D. Nordlund, M.F. Toney, J. Huang, Z. Bao, Ultra-high mobility transparent organic thin film transistors grown by an off-centre spin-coating method, Nat. Commun. 5 (2014) 3005, https://doi.org/10.1038/ncomms4005.

[12] S. Sanda, R. Nakamichi, T. Nagase, T. Kobayashi, K. Takimiya, Y. Sadamitsu, H. Naito, Effect of non-chlorinated solvents on the enhancement of field-effect mobility in dioctylbenzothienobenzothiophene-based top-gate organic transistors processed by spin coating, Org. Electron. 69 (2019) 181–189, https://doi.org/10.1016/j.orgel.2019.02.004.

[13] Z. Wang, H. Guo, J. Li, L. Wang, G. Dong, Marangoni effect-controlled growth of oriented film for high performance C8-BTBT transistors, Adv. Mater. Interfaces 6 (2019), 1801736, https://doi.org/10.1002/admi.201801736.

[14] D. He, Y. Pan, H. Nan, S. Gu, Z. Yang, B. Wu, X. Luo, B. Xu, Y. Zhang, Y. Li, Z. Ni, B. Wang, J. Zhu, Y. Chai, Y. Shi, X. Wang, A van der Waals pn heterojunction with organic/inorganic semiconductors, Appl. Phys. Lett. 107 (2015), 183103, https://doi.org/10.1063/1.4935028.

[15] L. Li, S. Tong, Y. Zhao, C. Wang, S. Wang, L. Lyu, Y. Huang, H. Huang, J. Yang, D. Niu, X. Liu, Y. Gao, Interfacial electronic structures of photodetectors based on C8BTBT/perovskite, ACS Appl. Mater. Interfaces 10 (2018) 20959–20967, https://doi.org/10.1021/acsami.8b03355.

[16] Y. Ni, J. Zhou, Y. Hao, H. Yu, Y. Wang, P. Gan, S. Hu, Effective performance improvement based on dioctylbenzothienobenzothiophene/pentacene isotype organic heterojunction transistors, Semicond. Sci. Technol. 34 (2019), 055003, https://doi.org/10.1088/1361-6641/ab0810.

[17] X. Liu, X. Luo, H. Nan, H. Guo, P. Wang, L. Zhang, M. Zhou, Z. Yang, Y. Shi, W. Hu, Z. Ni, T. Qiu, Z. Yu, J.-B. Xu, X. Wang, Epitaxial ultrathin organic crystals on graphene for high-efficiency phototransistors, Adv. Mater. 28 (2016) 5200–5205, https://doi.org/10.1002/adma.201600400.

[18] R. Miscioscia, F. Loffredo, G. Nenna, F. Villani, C. Minarini, M. Petrosino, A. Rubino, M. Denti, A. Facchetti, Analysis of the persistent photoresponse of C8BTBT transistors in the near-bandgap spectral region, Org. Electron. 30 (2016) 83–91, https://doi.org/10.1016/j.orgel.2015.11.029.

[19] I.G. Hill, D. Milliron, J. Schwartz, A. Kahn, Organic semiconductor interfaces: electronic structure and transport properties, Appl. Surf. Sci. 166 (2000) 354–362, https://doi.org/10.1016/S0169-4332(00)00449-9.

[20] Y. Diao, L. Shaw, Z. Bao, S.C.B. Mannsfeld, Morphology control strategies for solution-processed organic semiconductor thin films, Energy Environ. Sci. 7 (2014) 2145–2159, https://doi.org/10.1039/C4EE00688G.

[21] C. d. Dimitrakopoulos, P. r. l. Malenfant, Organic thin film transistors for large area electronics, Adv. Mater. 14 (2002) 99–117, https://doi.org/10.1002/1521-4095(20020116)14:2<99::AID-ADMA99>3.0.CO;2-9.

[22] A.O.F. Jones, B. Chattopadhyay, Y.H. Geerts, R. Resel, Substrate-induced and thin-film phases: polymorphism of organic materials on surfaces, Adv. Funct. Mater. 26 (2016) 2233–2255, https://doi.org/10.1002/adfm.201503169.

[23] T. Salzillo, A. Brillante, A new approach to polymorphism in molecular crystals: substrate-mediated structures revealed by lattice phonon dynamics, Adv. Mater. Interfaces 9 (2022), 2200815, https://doi.org/10.1002/admi.202200815.

[24] S. Riera-Galindo, F. Leonardi, R. Pfattner, M. Mas-Torrent, Organic semiconductor/polymer blend films for organic field-effect transistors, Adv. Mater. Technol. 4 (2019), 1900104, https://doi.org/10.1002/admt.201900104.

[25] T. Salzillo, A. Campos, A. Babuji, R. Santiago, S.T. Bromley, C. Ocal, E. Barrena, R. Jouclas, C. Ruzie, G. Schweicher, Y.H. Geerts, M. Mas-Torrent, Enhancing long-term device stability using thin film blends of small molecule semiconductors and insulating polymers to trap surface-induced polymorphs, Adv. Funct. Mater. 30 (2020), 2006115, https://doi.org/10.1002/adfm.202006115.

[26] T. Salzillo, N. Montes, R. Pfattner, M. Mas-Torrent, Selection of the two enantiotropic polymorphs of diF-TES-ADT in solution sheared thin film transistors, J. Mater. Chem. C 8 (2020) 15361–15367, https://doi.org/10.1039/D0TC03222K.

[27] I. Temiño, F.G. Del Pozo, M.R. Ajayakumar, S. Galindo, J. Puigdollers, M. Mas-Torrent, A. Rapid, Low-cost, and scalable technique for printing state-of-the-art organic field-effect transistors, Adv. Mater. Technol. 1 (2016), 1600090, https://doi.org/10.1002/admt.201600090.

[28] A. Pérez-Rodríguez, I. Temiño, C. Ocal, M. Mas-Torrent, E. Barrena, Decoding the vertical phase separation and its impact on C8-BTBT/PS transistor properties, ACS Appl. Mater. Interfaces 10 (2018) 7296–7303, https://doi.org/10.1021/acsami.7b19279.

[29] J. Li, A. Babuji, I. Temiño, T. Salzillo, F. D'Amico, R. Pfattner, C. Ocal, E. Barrena, M. Mas-Torrent, Chemical doping of the organic semiconductor C8-BTBT-C8 using an aqueous iodine solution for device mobility enhancement, Adv. Mater. Technol. n/a (n.d.) 2101535. https://doi.org/10.1002/admt.202101535.

[30] F. D'Amico, M. Saito, F. Bencivenga, M. Marsi, A. Gessini, G. Camisasca, E. Principi, R. Cucini, S. Di Fonzo, A. Battistoni, E. Giangrisostomi, C. Masciovecchio, UV resonant Raman scattering facility at Elettra, Nucl. Instrum. Methods Phys. Res. Sect. A 703 (2013) 33–37, https://doi.org/10.1016/j.nima.2012.11.037.

[31] A.D. Becke, Density-functional thermochemistry. IV. A new dynamical correlation functional and implications for exact-exchange mixing, J. Chem. Phys. 104 (1996) 1040–1046, https://doi.org/10.1063/1.470829.

[32] A.D. Becke, Density-functional thermochemistry. III. The role of exact exchange, J. Chem. Phys. 98 (1993) 5648–5652, https://doi.org/10.1063/1.464913.

[33] C. Lee, W. Yang, R.G. Parr, Development of the Colle-Salvetti correlation-energy formula into a functional of the electron density, Phys. Rev. B. 37 (1988) 785–789, https://doi.org/10.1103/PhysRevB.37.785.

[34] S.G. Balasubramani, G.P. Chen, S. Coriani, M. Diedenhofen, M.S. Frank, Y. J. Franzke, F. Furche, R. Grotjahn, M.E. Harding, C. Hättig, A. Hellweg, B. Helmich-Paris, C. Holzer, U. Huniar, M. Kaupp, A. Marefat Khah, S. Karbalaei Khani, T. Müller, F. Mack, B.D. Nguyen, S.M. Parker, E. Perlt, D. Rappoport, K. Reiter, S. Roy, M. Rückert, G. Schmitz, M. Sierka, E. Tapavicza, D.P. Tew, C. van Wüllen, V.K. Voora, F. Weigend, A. Wodyński, J.M. Yu, TURBOMOLE: modular program suite for ab initio quantum-chemical and condensed-matter simulations, J. Chem. Phys. 152 (2020), 184107, https://doi.org/10.1063/5.0004635.

[35] F. Weigend, R. Ahlrichs, Balanced basis sets of split valence, triple zeta valence and quadruple zeta valence quality for H to Rn: design and assessment of accuracy, Phys. Chem. Chem. Phys. 7 (2005) 3297–3305, https://doi.org/10.1039/B508541A.

[36] M.K. Kesharwani, B. Brauer, J.M.L. Martin, Frequency and zero-point vibrational energy scale factors for double-hybrid density functionals (and other selected methods): can anharmonic force fields be avoided? J. Phys. Chem. A 119 (2015) 1701–1714, https://doi.org/10.1021/jp508422u.

[37] T. Salzillo, A. Giunchi, M. Masino, N. Bedoya-Martínez, R.G. Della Valle, A. Brillante, A. Girlando, E. Venuti, An alternative strategy to polymorph recognition at work: the emblematic case of coronene, Cryst. Growth Des. 18 (2018) 4869–4873, https://doi.org/10.1021/acs.cgd.8b00934.

[38] N. Bedoya-Martínez, B. Schrode, A.O.F. Jones, T. Salzillo, C. Ruzié, N. Demitri, Y. H. Geerts, E. Venuti, R.G. Della Valle, E. Zojer, R. Resel, DFT-assisted polymorph identification from lattice Raman fingerprinting, J. Phys. Chem. Lett. 8 (2017) 3690–3695, https://doi.org/10.1021/acs.jpclett.7b01634.

[39] F. D'Amico, M.E. Musso, R.J.F. Berger, N. Cefarin, G. Birarda, G. Tondi, D. Bertoldo Menezes, A. Reyer, L. Scarabattoli, T. Sepperer, T. Schnabel, L. Vaccari, Chemical constitution of polyfurfuryl alcohol investigated by FTIR and Resonant Raman spectroscopy, Spectrochim. Acta A Mol. Biomol. Spectrosc. (2021), 120090, https://doi.org/10.1016/j.saa.2021.120090.

[40] F. D'Amico, F. Cammisuli, R. Addobbati, C. Rizzardi, A. Gessini, C. Masciovecchio, B. Rossi, L. Pascolo, Oxidative damage in DNA bases revealed by UV resonant Raman spectroscopy, Analyst 140 (2015) 1477–1485, https://doi.org/10.1039/C4AN02364A.

[41] F. Neese, The ORCA program system, WIREs Comput. Mol. Sci. 2 (2012) 73–78, https://doi.org/10.1002/wcms.81.

[42] T. Izawa, E. Miyazaki, K. Takimiya, Molecular ordering of high-performance soluble molecular semiconductors and *re*-evaluation of their field-effect transistor characteristics, Adv. Mater. 20 (2008) 3388–3392, https://doi.org/10.1002/adma.200800799.

[43] C. Kim, A. Jo, H. Kim, M. Kim, J. Lee, M.J. Lee, Solvent vapor annealing effects in contact resistances of zone-cast benzothienobenzothiophene (C8-BTBT) transistors,

J. Korean Ceram. Soc. 53 (2016) 411–416, https://doi.org/10.4191/kcers.2016.53.4.411.
[44] I. Deperasińska, M. Banasiewicz, P. Gawryś, O. Morawski, J. Olas, B. Kozankiewicz, Spectra and nature of the electronic states of [1]Benzothieno[3,2-*b*][1]benzothiophene (BTBT): single crystal and the aggregates, J. Chem. Phys. 155 (2021), 034504, https://doi.org/10.1063/5.0057202.
[45] Z. Hong, S.A. Asher, Dependence of Raman and resonance Raman intensities on sample self-absorption, Appl. Spectrosc. 69 (2015) 75–83.
[46] C.-M. Keum, S. Liu, A. Al-Shadeedi, V. Kaphle, M.K. Callens, L. Han, K. Neyts, H. Zhao, M.C. Gather, S.D. Bunge, R.J. Twieg, A. Jakli, B. Lüssem, Tuning charge carrier transport and optical birefringence in liquid-crystalline thin films: a new design space for organic light-emitting diodes, Sci. Rep. 8 (2018) 699, https://doi.org/10.1038/s41598-018-19157-9.
[47] M.S. Barclay, T.J. Quincy, D.B. Williams-Young, M. Caricato, C.G. Elles, Accurate assignments of excited-state resonance raman spectra: a benchmark study combining experiment and theory, J. Phys. Chem. A 121 (2017) 7937–7946, https://doi.org/10.1021/acs.jpca.7b09467.
[48] S.A. Asher, UV resonance Raman spectroscopy for analytical, physical, and biophysical chemistry. Part 1, Anal. Chem. 65 (1993) 59A–66A, https://doi.org/10.1021/ac00050a001.